Absolute instabilities in the spatially developing Kuroshio Extension

Article *in* Dynamics of Atmospheres and Oceans · January 2021

DOI: 10.1016/j.dynatmoce.2021.101205

Dynamics of Atmospheres and Oceans 93 (2021) 101205

Contents lists available at ScienceDirect

Dynamics of Atmospheres and Oceans

journal homepage: www.elsevier.com/locate/dynatmoce

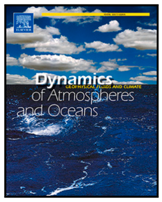

Absolute instabilities in the spatially developing Kuroshio Extension

X. San Liang [a,b,*], Jianyu Hu [a]

[a] *State Key Laboratory of Marine Environmental Science, College of Ocean and Earth Sciences, Xiamen University, Xiamen 361102, China*
[b] *Center for Ocean–Atmosphere Dynamical Studies, Nanjing Institute of Meteorology, Nanjing 210044, China*

ARTICLE INFO

Keywords:
Kuroshio Extension
Absolute instability
Convective instability

ABSTRACT

Satellite observations have long revealed to us a spatially growing Kuroshio Extension (KEx), but its underlying dynamics is yet to be studied. With a normal mode model of absolute/convective instability, it is found that the mean zonal jet is unstable at all the sections in the downstream region (east of 154 °E). In each of the resulting complex dispersion relation diagrams there lies a single saddle point associated with a positive temporal growth rate; that is to say, the mean jet is absolutely unstable, implying that KEx favors self-sustained oscillations. By calculation the absolute instability wave has a period increasing from about 27 days to 72 days, and a slightly decreasing wavelength from 360 km to 250 km, as longitude increases from 154 °E to 174 °E, agreeing with those inferred from the wavelet power spectra and Hovmöller diagram of the satellite observations. As KEx travels downstream, the associated eigen-structure of the perturbation velocity changes from a surface trapped mode to a mode with components maximized in the vertical interior. This study shows that at least a portion of the KEx intraseasonal variability is of intrinsic origin, and may be predictable with the absolute/convective instability theory.

1. Introduction

Kuroshio separates from the Japan Coast around (35°N, 140°E) and forms an eastward zonal jet, which eventually merges into the North Pacific Ocean Circulation. The part between 140–160°E is usually referred to as Kuroshio Extension, or KEx for short. KEx has been of interest for decades because of its importance in oceanography, climate science, and other disciplines. It transports heat into the interior of the Pacific Ocean, impacting significantly the climate over the North Pacific (Latif and Barnett, 1994; Schneider et al., 2002; Nakamura and Shimpo, 2004; Qiu et al., 2013; Wang and Liu, 2015; Wijffels et al., 1998). Its variability leads to the generation of mesoscale eddies, which are found to carry momentum and energy across the front, forming an important mechanism of transporting heat from the Tropics to high latitudes. These eddies also redistribute local nutrients, and hence exert influence on the local fishing grounds and ecosystems (Miller et al., 2004; Nishikawa and Yasuda, 2008, 2011; Sasai et al., 2010). For a recent review, see Kida and coauthors (2015).

KEx is highly variable; the variabilities form a broad spectrum (e.g., Mizuno and White, 1983), from submesoscale processes to mesoscale eddies, to decadal oscillations (e.g., Qiu, 2003) These variabilities may have different dynamical origins; differentiation of their generating mechanisms thence has become an important research field in the KEx studies. Generally speaking, they may be either remotely driven or of local origin(s). In previous studies the external contribution has been considered to be more important; particularly, many KEx variabilities have been related to the disturbances in the East Pacific Ocean and/or the wind stress anomalies above (e.g., Miller et al., 2004; Deser et al., 1999; Seager et al., 2001; Qiu, 2003; Kwon and Deser, 2007; Ceballos et al., 2009;

* Correspondence to: Center for Ocean–Atmosphere Dynamical Studies, Nanjing Institute of Meteorology, 219 Ningliu Blvd, Nanjing 210044, China.
E-mail address: sanliang@courant.nyu.edu (X.S. Liang).

https://doi.org/10.1016/j.dynatmoce.2021.101205
Received 30 April 2020; Received in revised form 17 December 2020; Accepted 24 January 2021
Available online 28 January 2021
0377-0265/

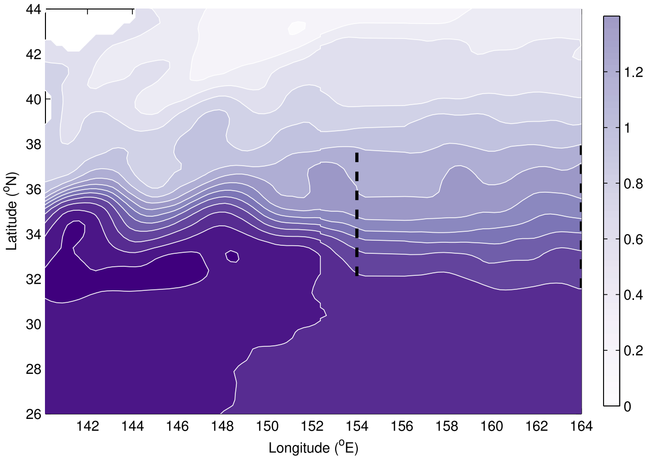

Fig. 1. The 22-year mean SSH (in meters) of the KEx region with the AVISO daily data for the period 1993–2015 (www.aviso.altimetry.fr). The two black dashed lines (resp. at 154°E and 164°E) will be used for spatial growth rate estimation.

Sasaki et al., 2012). Indeed, satellite observations seem to favor this opinion; the observed westward propagating Rossby waves are manifestation (e.g., Chelton and Schlax, 1996). On the other hand, it has also long been argued that the internal processes may be of equal importance (McCalpin and Haidvogel, 1996; Simonnet and Dijkstra, 2002; Hogg et al., 2005; Nonaka et al., 2006; Primeau and Newman, 2008; Penduff et al., 2011; Pierini, 2006, 2014; Pierini et al., 2009), and, actually, more fundamental from a viewpoint of geophysical fluid dynamics (Sasaki and Schneider, 2011). Moreover, some seemingly externally driven process may turn out to be intrinsic if viewed in a larger system. For example, on a decadal time scale, the KEx oscillation has been shown to be a self-sustained mode in an air–sea coupled model (Barnett et al., 1999; Qiu et al., 2013; Taguchi et al., 2010): An increase in Kuroshio transport increases the sea surface temperature (SST) in the KEx region and hence decreases the meridional SST gradient, which tends to reduce the global wind stress curl; the reduced wind stress curl then weakens the subtropical gyre, and hence reduces the Kuroshio transport, leading to an oscillation on the decadal scale (e.g., Latif and Barnett, 1994)

A conspicuous phenomenon about the KEx variability is its spatial development as well as its temporal growth. The sequence of the jet axis variation in Qiu and Chen (2010) provides a good illustration. From it one sees that, though differing year by year, the KEx oscillations generally amplify downstream. This is also implied in the envelopes of the long term mean AVISO sea surface height (SSH), as shown in Fig. 1. Dynamically this means that, in studying the instability problem, both temporal growth and spatial growth should be taken into account. The underlying instability, if existing, may be either convective or absolute. Disturbances generated from a convective instability will propagate away from their source(s); the system functions just like a noise amplifier. On the other hand, an absolute instability will produce disturbances powerful enough to counteract the propagation and become stationary, making the system a self-sustained oscillator. From a dynamical point of view, the latter is intrinsic and hence more fundamental. Considering the KEx variability as shown in Fig. 1, it is natural to ask whether the system admits absolute instability, and, if so, how frequency is selected. But, unfortunately, so far as of today these issues have been mostly overlooked.

We are therefore about to investigate the spatial development as well as the temporal growth, and accordingly the convective and absolute instabilities, in the hope of singling out from the broad KEx spectrum some variabilities of intrinsic origin(s). In the following we first formulate the problem, and give a brief introduction of the instability theory within the model framework. Section 3 presents the analysis results, and Section 4 provides the evidence from observations. This study is concluded in Section 5.

2. Formulation of the KEx convective/absolute instability problem

Convective and absolute instabilities have been well studied in physics (particularly in plasma physics)(e.g., Briggs, 1964; Bers, 1975; Lifshitz and Pitaevskii, 1981) and hydrodynamics (e.g., Chomaz et al., 1988; Huerre and Monkewitz, 1990; Pier, 2008). In oceanic and atmospheric dynamics, however, this is a relatively less explored field. Research works so far include Hogg (1976), Thacker (1976), Merkine (1977), Ikeda and Apel (1981), Lindzen and Farrell (1983), Pierrehumbert (1984), Held et al. (1986), Polvani and Pedlosky (1988), DelSole (1997), etc. Recently there have been an application to parameter tuning in numerical modeling (Liang and Robinson, 2013), and an exploration of the connection to El Niño (Thual et al., 2013). In this section, we first formulate the eigenvalue problem, then briefly introduce within the framework the basics about these instabilities.

Consider the primitive equation model that has been used in the Harvard Ocean Prediction System(cf. Robinson, 1999):

$$\frac{\partial u^*}{\partial t} + u^* \frac{\partial u^*}{\partial x} + v^* \frac{\partial u^*}{\partial y} + w^* \frac{\partial u^*}{\partial z} - f v^* = -\frac{1}{\rho_0} \frac{\partial P^*}{\partial x} + \nu_M \frac{\partial^2 u^*}{\partial z^2} + K_M \nabla^2 u^* \tag{1}$$

$$\frac{\partial v^*}{\partial t} + u^* \frac{\partial v^*}{\partial x} + v^* \frac{\partial v^*}{\partial y} + w^* \frac{\partial v^*}{\partial z} + f u^* = -\frac{1}{\rho_0} \frac{\partial P^*}{\partial y} + \nu_M \frac{\partial^2 v^*}{\partial z^2} + K_M \nabla^2 v^* \tag{2}$$

$$\frac{\partial P^*}{\partial z} = -\rho^* g \tag{3}$$

$$\frac{\partial u^*}{\partial x} + \frac{\partial v^*}{\partial y} + \frac{\partial w^*}{\partial z} = 0 \tag{4}$$

$$\frac{\partial \rho^*}{\partial t} + u^* \frac{\partial \rho^*}{\partial x} + v^* \frac{\partial \rho^*}{\partial y} + w^* \frac{\partial \rho^*}{\partial z} + w^* \frac{d\rho_s}{dz} = \nu_T \frac{\partial^2 \rho^*}{\partial z^2} + K_T \nabla^2 \rho^*, \tag{5}$$

where all the state variables are starred for later convenience. Here ρ^* is the density anomaly ($\rho_{original} - 1000$ kg/m^3) with the horizontally and temporally averaged profile $\rho_s(z)$ removed; x directs eastward, y northward, and z upward; the subscripts T and M for the eddy viscosities stand for "tracer" and "momentum", respectively. The other notations are conventional and can be found in standard geophysical fluid dynamics textbooks such as Pedlosky (1979).

Integrating the hydrostatic equation, one obtains

$$P^*(z) = P^*(-H) + \int_{-H}^{z} (-\rho^* g) dz.$$

Here $P^*(-H)$ is the pressure at depth H; it may be taken as spatially invariant in many problems. This is actually what is done in reduced gravity models, where the infinitely deep layer has a constant pressure. (With a finite flux, the infinite depth implies a zero flow, and by geostrophy the pressure gradient must vanish.) In the KEx problem, provided that H is large enough, this is appropriate, as we will see soon in the next section, the jet is limited in the upper 1000 meters or so. Thus

$$\nabla P^* = -g \int_{-H}^{z} \nabla \rho^* dz, \tag{6}$$

where ∇ signifies horizontal gradient. Further assuming a rigid lid, which is appropriate in this context (e.g., Pedlosky, 1979), we have

$$w^* = -\int_0^z \left(\frac{\partial u^*}{\partial x} + \frac{\partial v^*}{\partial y} \right) dz. \tag{7}$$

The two substituted back to the primitive equations result in an integro-differential equation set with the three prognostic variables (u^*, v^*, ρ^*). With appropriate boundary conditions, the equation set is closed and can be solved.

We want to study the behavior of the solution around some mean state $(\bar{u}, \bar{v}, \bar{\rho})$, which depends on (y, z) only. A simpler configuration but appropriate for the KEx study is

$$(\bar{u}, \bar{v}, \bar{\rho}) = (\bar{u}(y, z), 0, \bar{\rho}(y, z)). \tag{8}$$

This is justified by the relatively straight jet stream in question (observe the segment between the dashed lines in Fig. 1). The basic profile will be derived from the "Estimating the Circulation and Climate of the Ocean" dataset, which will be shown in Section 3.1. Notice that $\bar{u}$ and $\bar{\rho}(y, z)$ must meet some dynamical constraint(s); here it is the thermal wind relation.

Perturb the system from the mean state:

$$\rho^* = \bar{\rho} + \rho',$$
$$u^* = \bar{u} + u',$$
$$v^* = \bar{v} + v' = v'.$$

Linearizing, we get

$$\frac{\partial u'}{\partial t} + \bar{u}\frac{\partial u'}{\partial x} + v'\frac{\partial \bar{u}}{\partial y} - \frac{\partial \bar{u}}{\partial z}\int_0^z \left(\frac{\partial u'}{\partial x} + \frac{\partial v'}{\partial y} \right) dz - f v' = \frac{g}{\rho_0}\int_{-H}^{z} \frac{\partial \rho'}{\partial x} dz + \nu_M \frac{\partial^2 u'}{\partial z^2} + K_M \nabla^2 u' \tag{9}$$

$$\frac{\partial v'}{\partial t} + \bar{u}\frac{\partial v'}{\partial x} + f u' = \frac{g}{\rho_0}\int_{-H}^{z} \frac{\partial \rho'}{\partial y} dz + \nu_M \frac{\partial^2 v'}{\partial z^2} + K_M \nabla^2 v' \tag{10}$$

$$\frac{\partial \rho'}{\partial t} + \bar{u}\frac{\partial \rho'}{\partial x} + v'\frac{\partial \bar{\rho}}{\partial y} - \left(\frac{\partial \bar{\rho}}{\partial z} + \frac{d\rho_s}{dz} \right)\int_0^z \left(\frac{\partial u'}{\partial x} + \frac{\partial v'}{\partial y} \right) dz = \nu_T \frac{\partial^2 \rho'}{\partial z^2} + K_T \nabla^2 \rho' \tag{11}$$

Assuming a solution of the form

$$(u', v', \rho') = (u, v, \rho) e^{i(\sigma t - kx)}, \tag{12}$$

the above equations are reduced to:

$$\begin{aligned} &\left(\frac{\partial \bar{u}}{\partial y} - f \right) v + \frac{\partial \bar{u}}{\partial z}\int_0^z \left(iku - \frac{\partial v}{\partial y} \right) dz \\ &\qquad - K_M \frac{\partial^2 u}{\partial y^2} - \nu_M \frac{\partial^2 u}{\partial z^2} + ik\frac{g}{\rho_0}\int_{-H}^{z} \rho dz \\ &= -(i\sigma - ik\bar{u} + k^2 K_M) u, \end{aligned} \tag{13}$$

$$\begin{aligned} &f u - K_M \frac{\partial^2 v}{\partial y^2} - \nu_M \frac{\partial^2 v}{\partial z^2} - \frac{g}{\rho_0}\int_{-H}^{z} \frac{\partial \rho}{\partial y} dz \\ &= -(i\sigma - ik\bar{u} + k^2 K_M) v, \end{aligned} \tag{14}$$

$$\frac{\partial\bar{\rho}}{\partial y}v + \left(\frac{\partial\bar{\rho}}{\partial z} + \frac{d\rho_s}{dz}\right)\int_0^z \left(iku - \frac{\partial v}{\partial y}\right)dz$$
$$-K_T\frac{\partial^2\rho}{\partial y^2} - \nu_T\frac{\partial^2\rho}{\partial z^2}$$
$$= -(i\sigma - ik\bar{u} + k^2K_T)\rho. \tag{15}$$

Here both k and σ are complex:

$$k = k_r + ik_i, \qquad \sigma = \sigma_r + i\sigma_i.$$

Note in (12), the spatial growth rate (in positive x) is k_i, but the temporal growth rate is $-\sigma_i$. These equations, together with the simple zero-gradient conditions for both vertical and horizontal boundaries:

$$\frac{\partial u}{\partial z}, \frac{\partial v}{\partial z}, \frac{\partial \rho}{\partial z} = 0 \qquad \text{at } z = 0,\ -H \tag{16}$$
$$\frac{\partial u}{\partial y}, \frac{\partial v}{\partial y}, \frac{\partial \rho}{\partial y} = 0 \qquad \text{at } y \text{ boundaries} \tag{17}$$

(equivalent to no mass fluxes across the surface and bottom, and no wind forcing), form an eigenvalue problem. Here the y-boundary conditions are justified by the observation that the jet flows mostly eastward. Particularly, if $\bar{u} = \text{constant}$, $K_M = K_T$, then $(i\sigma - ik\bar{u} + k^2K_M)$ is the eigenvalue.

An observation about the system is that dissipation/diffusion (K_M or K_T) generally inhibits temporal growth, since for a real k, k^2 is always positive, and hence k^2K_M functions to inhibit the disturbance growth. However, when spatial growth is considered, k has an imaginary part, k^2K_M may become negative; that is to say, dissipation may trigger absolute instability. This is an interesting topic which has been examined before (e.g., DelSole, 1997; Held et al., 1986; Polvani and Pedlosky, 1988).

In general, Eqs. (13)–(15) can only be solved numerically. We discretize them on a grid with uniform horizontal mesh and variable spacings in z. The discretized equations admit nontrivial solutions only when k and σ satisfies a dispersion relation. Details of the discretization and solution for this study are deferred to Section 3.1. Here we symbolically write it as

$$\mathscr{L}(\sigma, k) = 0. \tag{18}$$

This relation in spectral space corresponds to an integro-differential operator $\mathscr{L}(-i\partial/\partial t, i\partial/\partial x)$ in physical space. Let the eigenfunction of the perturbation fields (u', v', ρ') be $\phi(x,t)$. Then,

$$\mathscr{L}\left(-i\frac{\partial}{\partial t}, i\frac{\partial}{\partial x}\right)\phi(x,t) = 0. \tag{19}$$

Now look at the response of the system to an impulse applied at the origin of the spacetime (x,t), i.e., the Green's function $G(x,t)$ such that

$$\mathscr{L}\left(-i\frac{\partial}{\partial t}, i\frac{\partial}{\partial x}\right)G(x,t) = \delta(x)\delta(t). \tag{20}$$

The convective/absolute instability is defined with the behavior of $G(x,t)$; see, for example, Huerre and Monkewitz (1990). Specifically, the background flow (8) is said to be linearly unstable if $\lim_{t\to\infty} G(x,t) = \infty$ along at least one ray $x/t = \text{constant}$; otherwise it is linearly stable. For linearly unstable flows, two cases are distinguished along the particular ray $x/t = 0$:

(1) $\lim_{t\to\infty} G(x,t) = 0;$

(2) $\lim_{t\to\infty} G(x,t) = \infty.$

In case (1), one observes at a fixed point (finite x) and finds that the disturbance gradually disappears; the disturbance is swept downstream. This type of instability is said to be *convective*. On the other hand, the disturbance in case (2) keeps growing even viewing from a fixed point. This type of instability is powerful enough to counteract the propagation and grow in all directions; it is called *absolute instability*.

The above definition is straightforward. But practically it is difficult to use. In plasma physics, a common practice is to identify the saddle point(s) as the spatial branches of the dispersion relation pinch on the complex k plane (e.g., Briggs, 1964; Bers, 1975). Details are referred to the comprehensive review Huerre and Monkewitz (1990) and other references such as Pierrehumbert (1984). The following supplies a brief summary.

Observe that Eq. (20) actually can be solved. Application of a Fourier transform on both sides, followed by an inverse Fourier transform, yields the Green function $G(x,t)$ in terms of a double Fourier integral

$$G(x,t) = \frac{1}{(2\pi)^2}\int_K\int_S \frac{e^{i(\sigma t - kx)}}{\mathscr{L}(\sigma,k)}d\sigma dk. \tag{21}$$

The choice of the contours S and K will be clear soon. Notice the integrand is singular on the curve(s) of dispersion. Assume a temporal mode $\sigma = \sigma(k)$. By Cauchy's residue theorem, the integral is

$$G(x,t) = -\frac{i}{2\pi}\int_{-\infty}^{+\infty}\frac{e^{i(\sigma(k)t - kx)}}{\partial\mathscr{L}/\partial\sigma(\sigma(k),k)}dk, \qquad t > 0. \tag{22}$$

As $t \to \infty$, this can be evaluated using the stationary phase approximation (e.g., Wong, 2001)

$$G(x,t) \approx -\frac{1}{\sqrt{2\pi}} e^{i\pi/4} \frac{e^{i(\sigma(k_*)t - k_* x)}}{\partial \mathscr{L}/\partial\sigma[k_*, \sigma(k_*)]\sqrt{\frac{\partial^2\sigma}{\partial k^2}(k_*)t}} \tag{23}$$

where k_* is such that

$$\left.\frac{\partial\sigma}{\partial k}\right|_{k_*} = \frac{x}{t}. \tag{24}$$

Following the peak of the wave packet, the maximal growth rate $-\sigma_{m,i}$ is attained at k_m such that

$$\frac{\partial\sigma_i}{\partial k} = 0, \qquad \text{for } k \text{ real.} \tag{25}$$

From (24),

$$\left.\frac{\partial\sigma_r}{\partial k}\right|_{k_m} = \frac{x}{t}. \tag{26}$$

That is to say, the peak of the most unstable wave packet moves at the group velocity at that wavenumber, i.e., $k_{\max}$.

For linearly unstable flow, we further look at its behavior at some fixed finite x as $t \to \infty$. We are particularly interested in the wavenumber k_0 such that

$$\left.\frac{\partial\sigma}{\partial k}\right|_{k_0} = 0, \qquad \text{as } x/t \to 0. \tag{27}$$

Correspondingly let the frequency be σ_0. We then have the following criterion:

- The basic flow is linearly unstable if $-\sigma_{m,i} > 0$;
- for linearly unstable flow, if $-\sigma_{0,i} > 0$, it is absolutely unstable; otherwise it is convectively unstable.

Note that $-\sigma_{0,i} \le -\sigma_{m,i}$, as established before (see references in Huerre and Monkewitz, 1990).

It has been shown that, in the σ-plane, the absolute frequency σ_0 is an algebraic branch point of $k(\sigma)$, while in the k-plane, k_0 is a saddle point (e.g., Huerre and Monkewitz, 1990). This provides an easy way to identify absolute instability, which is credited to Briggs (1964). For the purpose of illustration, suppose that $\sigma = \sigma(k)$ is a quadratic function in k. Thus there are two spatial branches; call them $k^+(\sigma)$ and $k^-(\sigma)$, as sketched in Fig. 2. Let us go back to (21). The paths S and K cannot be just chosen arbitrarily. S is a contour parallel to the σ_r axis. It must be above all the singularities of the integrand to meet the causality requirement, that is, $G = 0$ when $t < 0$. Correspondingly K takes a path initially coincident with the real axis in the complex k-plane. As S is displaced downward, the spatial branches are getting closer; particularly, $k^+(\sigma)$ or $k^-(\sigma)$ may cross the k_r axis. K must then be deformed to avoid trespassing the spatial branches. As k^+ and k^- are pinching they will eventually meet, say, at k_0, a saddle point where K passes. Correspondingly on the σ-plane $\sigma(k)$ also varies; it takes a cusp form at σ_0, the point where S stops. The imaginary part of σ_0 is the very $\sigma_{0,i}$ as discussed above for distinguishing convective and absolute instabilities. As an example, in the schematic $-\sigma_{0,i} > 0$, so the flow is absolutely unstable. Furthermore, $k_{0,i} > 0$; it thus amplifies toward the positive direction of x.

3. Temporal and spatial growths in the KEx region

3.1. Data and basic flow

We use for the analysis the data from the *Estimating the Circulation and Climate of the Ocean* (ECCO) group (www.ecco-group.org). The reason to choose it is because of its dynamical consistency in the course of integration, which is of essence for our study. The time period is from January 1, 1993, to December 31, 2014, with a resolution of 1 day. Average the fields over the period to obtain the mean profiles. In the vertical direction, the data are interpolated to the following 12 depths (in m): 50, 150, 250, 350, 450, 550, 650, 750, 850, 950, 1060, 1200. We use a grid with a uniform mesh in y but with variable spacings in z, and hence this results in 10 vertical spacings (Δz) of 100 m, plus two bottom spacings of 120 m and 160 m. (Note the depths should be carefully chosen, or the nonuniform mesh grid in z may result in negative Δz's.) The bottom level at 1200 m is deep enough to have $\bar{u}$ nearly vanishing (cf. Fig. 3), meeting the assumption of an inert bottom layer for the model.

Meridionally the domain is between 29.625–40.125°N, with a spacing of 0.5°. The non-integer latitudes coincide with the original data points. From Fig. 1, the KEx axis west of 150°E is not straight, which is beyond the capability of the present model. Thus, only the eastern part is considered for this study. Particularly we will focus our attention between 154–164°E, as from the figure even the segment between 150–155°E is much influenced by the meandering. In Fig. 3 the profiles of $\bar{\rho}(y,z)$ and $\bar{u}(y,z)$ at 154°E are shown. Note that the resulting $\bar{\rho}$ may not be consistent with $\bar{u}$. We hence recompute $\bar{\rho}$ from $\bar{u}$ using the thermal wind relation. The integration is from the southernmost boundary, where $\bar{\rho}$ is prescribed. The re-computed or rectified $\bar{\rho}$ is drawn in Fig. 3c. As can be seen, the two are essentially the same, though little difference does exist in regions of large $|\partial\bar{u}/\partial y|$.

We have drawn the mean profiles every two degrees eastward from 150°E; they only vary on a large scale. For example, Fig. 4 gives the profiles at 164°E.

Before proceeding, the two parameters in the model, namely, ν_M and K_M, need to be set. (ν_T and K_T are chosen to be the same as, respectively, ν_M and K_M.) It is found that a reasonable ν_M essentially has no affect on the result; we choose it to be

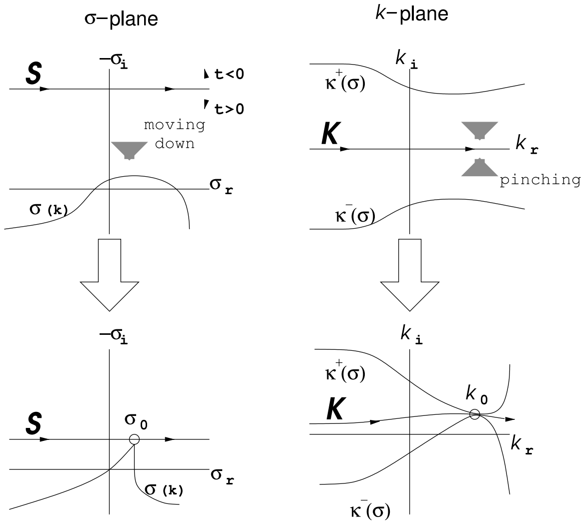

Fig. 2. A schematic of the pinching process on the complex k-plane (right panel) as the contour L is displaced downward in the complex σ-plane (left panel). Note the ordinate of the σ-plane is $-\sigma_i$, which is the temporal growth rate by (12). See Huerre and Monkewitz (1990) for more details.

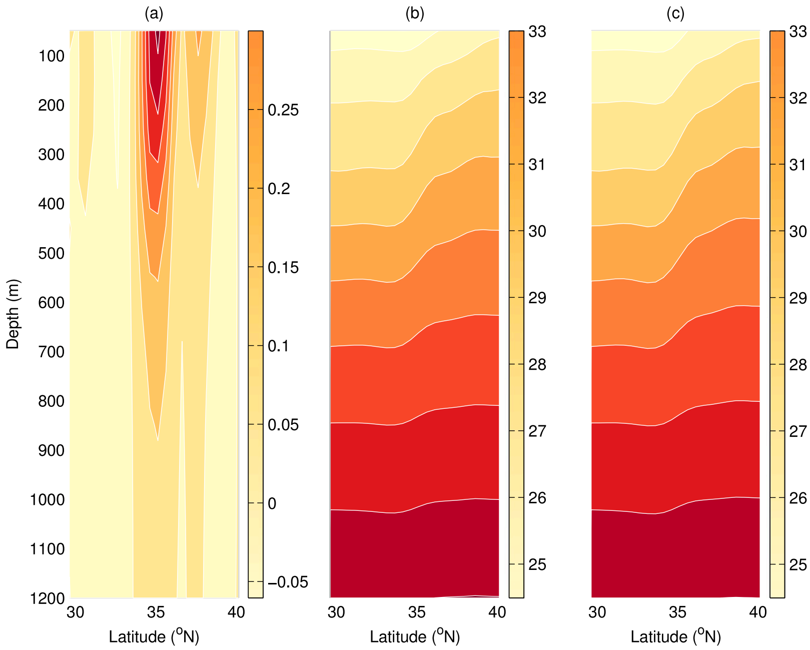

Fig. 3. Basic profiles for the instability model at 154°E: (a) $\bar{u}$ (in m/s), (b) $\bar{\rho}$ (density anomaly), (c) density anomaly in conformity with $\bar{u}$ through thermal wind relation.

$\nu_M = 5 \times 10^{-4}$ m^2/s. As we mentioned in the preceding section, K_M generally will inhibit the temporal growth. In this study, we find that, provided that K_M is not extremely large, it only slightly affects the growth rates (no qualitative change), with little influence on the wave properties. In the following presentation a relatively weak dissipation $K_M = 100$ m^2/s is chosen.

The above discretized system is solved by calling the LINPACK Fortran library (http://www.netlib.org/linpack/). As shown in Section 2, given a k, we can obtain a list of ordered eigenvalues. The one that maximizes the temporal growth rate is kept, and its corresponding eigenvector saved. By varying k, the dispersion relation is hence obtained.

3.2. Dispersion relation

From 150°E eastward till 174°E, we have performed the instability analysis for sections every 2° longitude, which totals 13 sections. Here we select out a couple of typical sections to illustrate.

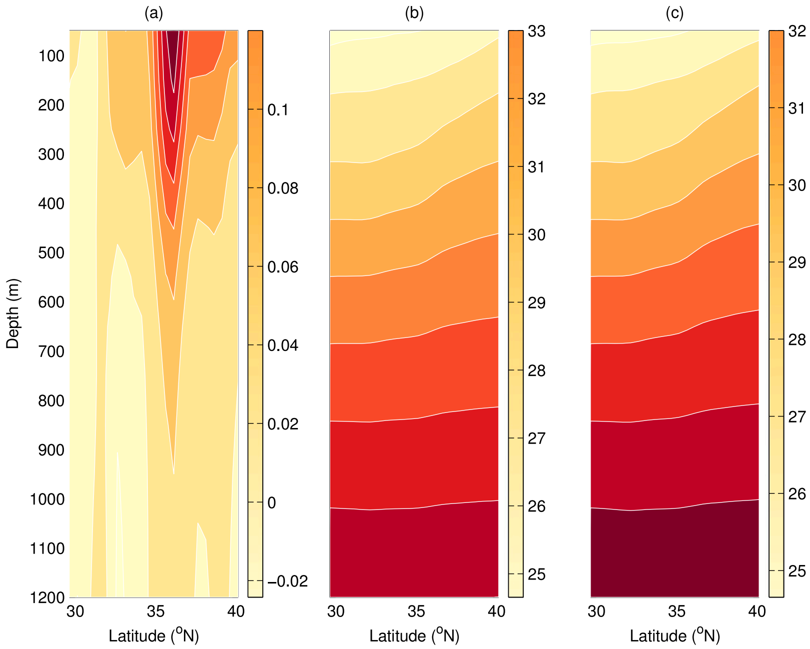

Fig. 4. As Fig. 3, but for 164°E.

3.2.1. *Section at 154°E*

Eqs. (13)–(15) together with the boundary conditions are solved for the dispersion relation. The growth rate $-\sigma_i$ as a function of k_r is plotted in Fig. 5a. We see that it has two maxima for $k_r > 0$, and there are another two for negative k_r values located symmetrically about $k_r = 0$. From the figure, $-\sigma_{m,i} = 6.2 \times 10^{-7} > 0$; the flow is hence locally unstable in the linear sense. In Fig. 5b, the branches of $-\sigma_{0,i} = 6.012 \times 10^{-7}$ pinch at the saddle point $k = (\pm 1.75 \times 10^{-5}, 1.25 \times 10^{-7})$. Since $-\sigma_{0,i} > 0$, the instability is absolute.

The absolute instability wave has a frequency $\sim 2.65 \times 10^{-6}$, which is approximately 27 days. The wave may propagate in both $+x$ and $-x$ directions, with a wavelength of $2\pi/1.75 \times 10^{-5}/1000 \approx 360$ km. It is spatially amplifying toward $+x$ direction, with a spatial growth rate of 1.25×10^{-7} m^{-1}.

3.2.2. *Sections at 164°E and further downstream*

For the section at 164°E, the dispersion structure has changed a little bit from the above. Fig. 6a shows the distribution of $-\sigma_i$ with k_r. Compared with Fig. 5a, still there exist two symmetric maxima, but the third and fourth maxima disappear. Since $-\sigma_{m,i} = 2.58 \times 10^{-7} > 0$, the basic flow at this longitude is also linearly unstable. From Fig. 6b we see that the two branches of $-\sigma_{0,i} = 2.537 \times 10^{-7}$ pinch at

$$k = (k_r, k_i) = (\pm 1.75 \times 10^{-5}, 0.5 \times 10^{-7})\ \mathrm{m}^{-1}.$$

This is the saddle point we are interested in, which corresponds to the temporal mode σ_0. Since $-\sigma_{0,i} > 0$, this is also an absolute instability.

Again the absolute instability wave may propagate in both direction. It has a wavelength of $2\pi/1.75 \times 10^{-5}/1000 = 360$ km, and a spatial growth rate of 0.5×10^{-7} m^{-1}. The real part of σ_0, i.e., $\sigma_{0,r}$, is by calculation 1.269×10^{-6} s^{-1}, which approximately corresponds to 57 days.

For sections further downstream, they are actually not KEx any more. We have examined several of them for comparison purposes. Generally, the dispersion relation seems to be qualitatively similar to that at 164°E; all admit absolute instabilities. For example, the section at 174°E has a dispersion curve similar to Fig. 6, save for a much smaller growth rate. To summarize, Table 1 lists the computed properties for different sections. Note that the results for the two sections at 150°E and 174°E may not be accurate enough. The former is close to a meandering jet. The latter has a broad jet, part of which already touches the computational domain.

3.3. *Eigenfunction*

Associated with the absolutely unstable modes are the eigenvectors. Contoured in Fig. 7 are the corresponding perturbation fields of u, v, and ρ at 154°E. Generally speaking, they are trapped in upper layers, though the real part of ρ may extend to a depth of 1100 m. An observation is that, while the velocity perturbation tends to be surface intensified, the density fluctuation has a double-maximum structure. Aside from the surface maximum, between 200 m and 400 m there exists a second one, which is obvious on both the real and imaginary distributions of ρ (Fig. 7c and f).

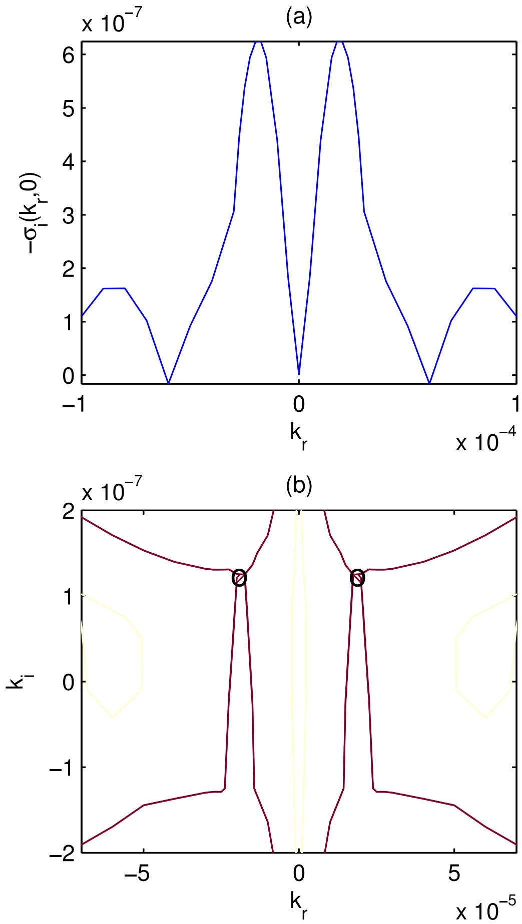

Fig. 5. Dispersion relation for section 154°E. (a) The temporal growth rate as function of real k. (b) The pinching of the two branches of $-\sigma_i = 6.012 \times 10^{-7}$ s^{-1}.

Table 1
Computed properties for the local absolute instability waves.

Longitude	Wavelength (km)	Period (days)	Spatial growth rate (m^{-1})	Temporal growth rate (s^{-1})
150°E	360	23	1.5×10^{-7}	7.1×10^{-7}
154°E	360	27	1.25×10^{-7}	6.012×10^{-7}
164°E	360	57	0.5×10^{-7}	2.537×10^{-7}
174°E	251	72	0.25×10^{-7}	1.66×10^{-7}

The unstable model at 164°E displays a quite different vertical structure. As seen from Fig. 8, the perturbations are not all trapped in upper layers. The real part of u and the imaginary part of v are mainly distributed between 300 m and 1000 m. Besides, the latitudinal structure is also different. For example, in Fig. 7c and f, ρ somehow has a solitary wave structure, but Fig. 8c and f show a structure with one or two peak(s) and one valley in y. Similar difference is also seen between the u_i's at the two sections (Figs. 7d and 8d).

In Fig. 8, it is seen that, in terms of vertical structure, u_r is related to v_i, and so is u_i to v_r. This is a manifestation of geostrophic balance, which reduces the continuity equation to

$$-iku + \frac{\partial v}{\partial y} = 0$$

in the present context. Thus a surface-trapped $Re\{u\}$ corresponds to a surface-trapped $Im\{v\}$, while an interior mode of $Im\{u\}$ corresponds to an interior mode of $Re\{v\}$.

4. Observational evidence

The absolute instabilities actually are evidenced in observations. In this section we look at the AVISO daily SSH series, which are available at www.aviso.altimetry.fr.

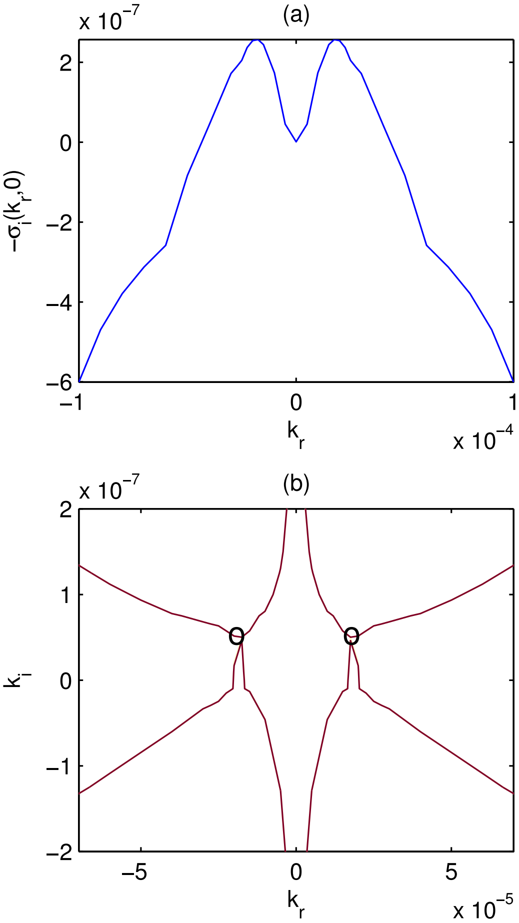

Fig. 6. Dispersion relation at 164°E. (a) The temporal growth rate as function of real k. (b) The pinching of the two branches of $-\sigma_i = 2.53 \times 10^{-7}$ s^{-1}.

4.1. Data pretreatment

The AVISO daily data are available from January 1, 1993, to present. As detailed in the following, the series should have a length of the power of 2, so we choose $2^{13} = 8192$ days starting from 01/01/1993, which result in a series ending in June 2015. In order to enhance the variabilities that interest us, the series are pretreated with the mean, linear trend, and annual variabilities removed.

4.2. Hovmöller diagram

Hovmöller diagrams are conventionally used to infer wave properties. We now examine the Hovmöller diagram of the fluctuations along the KEx axis. For this purpose, we first need to single out the processes with periods approximately between 30–70 days. This is achieved with the new machinery multiscale window transform (MWT) developed by Liang and Anderson (2007).

MWT is a functional analysis tool which decomposes a function space into a direct sum of orthogonal subspaces, each with an exclusive range of scales, while preserving its local properties. Such a subspace is termed a scale window, or simply a window. MWT is originally developed for a faithful representation of the multiscale energies (or any quadratic properties) on the resulting scale windows, and hence make multiscale energetics analysis possible. This is a feature lacked in the traditional filters, the outputs of which are fields in physical space, while multiscale energy is a concept in phase space which is connected to its physical space counterpart through the Parseval equality in functional analysis. Liang and Anderson (2007) realized that, just as the Fourier transform and inverse Fourier transform, there exists a transfer-reconstruction pair for a subclass of specially devised orthogonal filters. This motivates the introduction of MWT and its counterpart, multiscale window reconstruction (MWR). MWT/MWR and orthonormal wavelet transform are all based on multi-resolution analysis, but they are different by construction. MWR functions like a filter, while MWT outputs transform coefficients which can be combined into the different multiscale energetic terms.

In MWT/MWR, the scale windows are demarcated by scale level bounds. For a series with a time span of τ, a scale level j corresponds to a period $2^{-j}\tau$. The time steps of the series hence need to total to a number of the power of 2. As said above, the

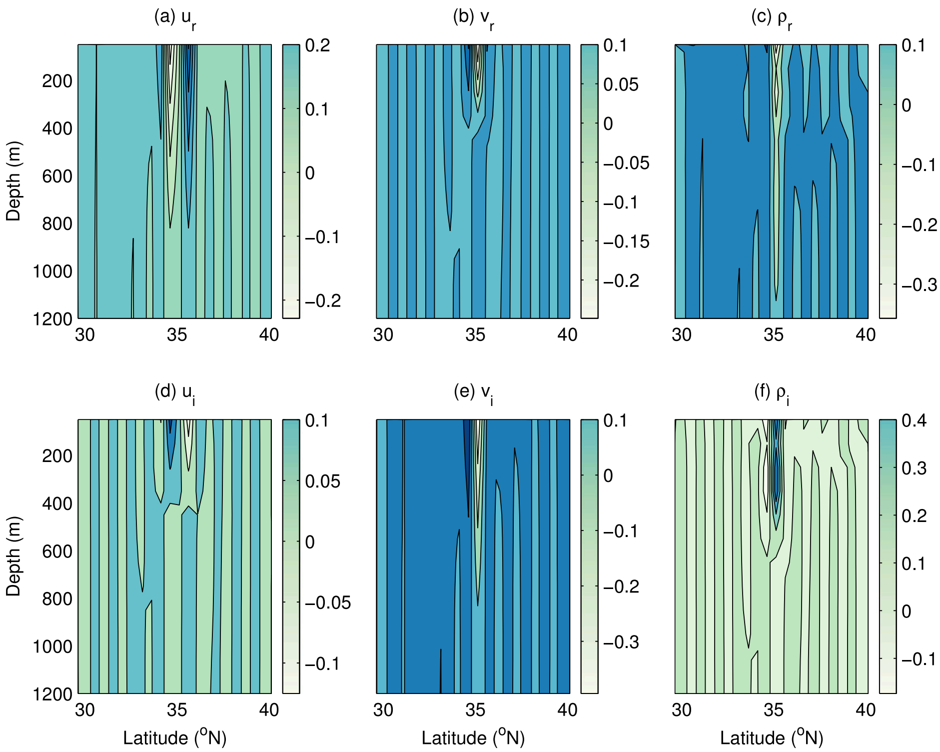

Fig. 7. Eigenfunction of the absolutely unstable mode at 154°E.

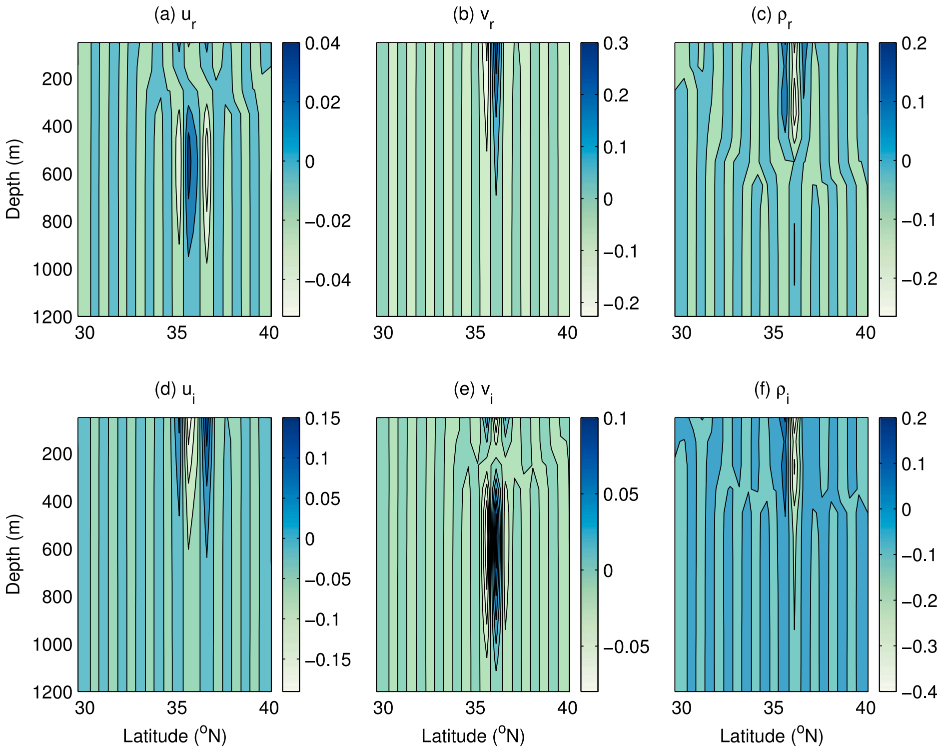

Fig. 8. Eigenfunction of the absolutely unstable mode at 164°E.

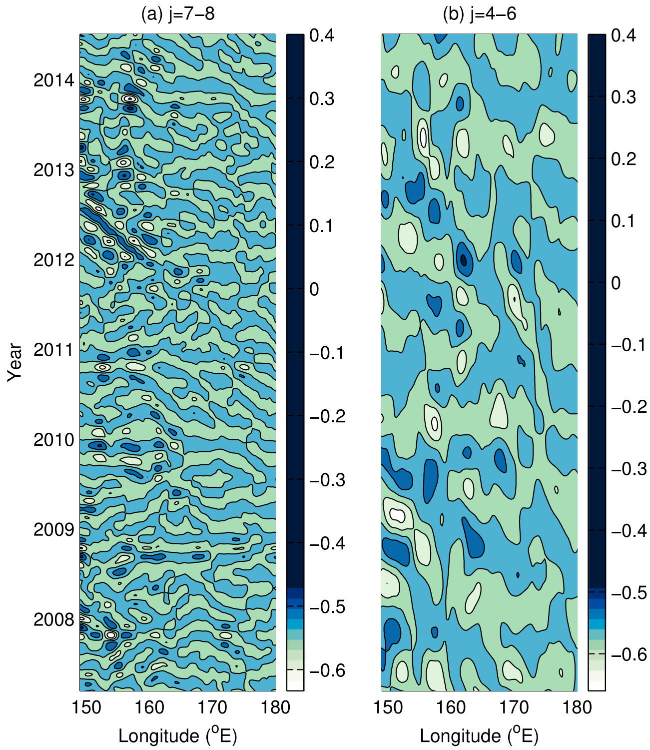

Fig. 9. The Hovmöller diagram of fluctuations on scale window (a) $j = 7 - 8$ and (b) $j = 4 - 6$.

AVISO series are chosen to have $2^{13} = 8192$ data points (days). Considering that the periods are around 30–70 days, we choose a window with scale level bounds $j = 7 - 8$ (corresponding to 64 and 32 days) and perform the multiscale window reconstruction. For easy reference, this window will be referred to as the absolute instability window henceforth.

From Fig. 1, the KEx axis in this region is at about 33°N. We choose 33.125°N, the nearest latitude where the AVISO daily data are available, to perform the reconstruction. We then draw the Hovmöller diagram of the reconstructed SSH for the period 01/01/1993–12/31/2015. Fig. 9 is a zoom of the diagram for 2007–2015.

It has long been observed that disturbances in North Pacific propagate westward in the form of Rossby waves; see, for example, Chelton and Schlax (1996). We have checked this with fluctuations reconstructed on scale windows larger than the absolute instability window, and things are indeed like that; Fig. 9b gives an example with $j = 4 - 6$ (corresponding to 1.4 year-4.2 months). However, on the absolute instability window ($j = 7 - 8$), a quite different scenario appears. In Fig. 9a, the propagation is not always westward. In many time periods, e.g., 2009, 2010–2011, 2013–2014, the waves may become stationary. This is the very indication of the absolute instability. Besides, there may even exist eastward propagations in Fig. 9a, agreeing with our model result that the instability waves may propagate in both directions.

4.3. Spatial growth rate and spatial scale

Originally it is the spatial growth that motivates this research. Let us see how it may be compared to the instability model prediction. Here we only look at the downstream region, since the upstream KEx variability is much influenced by the large meandering, which is beyond the capability of the present model. As marked in Fig. 1, choose the two contour lines 0.6 and 1.2. The two dashed lines, respectively located at 154°E and 164°E, are separated by 10° or 920 km at that latitude. The right line is roughly 1.1 times the left one. Let the growth rate be λ, then $\frac{dy}{dx} = \lambda y$, $\frac{y}{y_0} = e^{\lambda \Delta x}$. As $y/y_0 \approx 1.1$, $\Delta x = 9.2 \times 10^5$ m, $\lambda = \log_e 1.1/\Delta x = 1.04 \times 10^{-7}\ \mathrm{m}^{-1}$. This value lies between the spatial growth rates at 154°E ($k_i = 1.25 \times 10^{-7}\ \mathrm{m}^{-1}$) and 164°E ($0.5 \times 10^{-7}\ \mathrm{m}^{-1}$) as predicted by the instability model; it is very close to the former.

A property that is suitable for visual inspection is the eddy size. But here it is not an easy task to extract the information for an objective comparison. The reason is that, in the scale window of concern, the processes need not all be instabilities waves; other waves/eddies may also live in there.

Using the SSH fluctuations reconstructed above, we look at their Fourier spectrum along the KEx axis (between 150°E and 180°E). The spectrum is found to vary from time to time. Fig. 10 shows the variation during 2000–2015. Indeed, in this window there exist processes with very long spatial scales. But generally there is another peak, varying from $k/2\pi = 0.001$ (1000 km) to 0.003 (333 km). The long-time mean is approximately at 0.0015–0.00175 (570–670 km), which is much larger than that by model

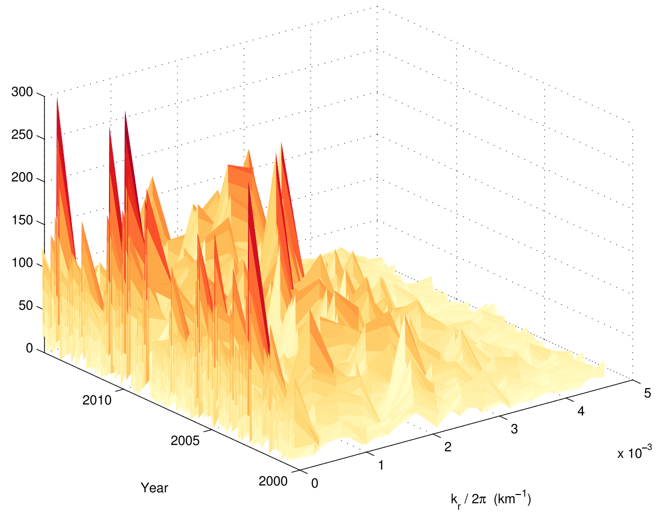

Fig. 10. The Fourier spectrum of the AVISO SSH along 33.125°N during 2000–2015.

prediction. However, there do exist periods when the second peak is placed at larger wavenumbers. By visual inspection a very clear peak around 2010 is between 0.0025–0.003, which corresponds to a spatial scale between 330–400 km. This is in agreement with the model prediction, i.e., 360 km.

To aid the visualization, we draw in Fig. 11a the horizontal distribution of a typical reconstructed SSH during this period: the distribution on the Christmas Day of 2010. By comparison both the amplitude and scale of the eddies are much smaller in the eastern region. While the amplitude distribution cannot be inferred with a linear wave theory, the spatial scale distribution does agree with our previous prediction, which gives a smaller wavelength in the east. To see it more clearly, we zoom in on the enhanced eddy region and plot it in Fig. 11b. The dipole in the east provides a nice paradigm for a wave. It straddles over about 4 longitudes, or $4 \times \pi/180 \times 6370 \times \cos 35° \approx 364$ km. This is almost the same as the 360 km as previously predicted for that longitudinal range.

4.4. Wavelet power spectra

Evidence also exists in power spectra. We pick out three longitudes: 154°E, 164°E, and 174°E on the above latitude 33.125°N to form three time series, and check the respective power spectra. The spectral analysis is with the orthonormalized wavelet basis built in (Liang and Anderson, 2007). (We have also performed a Fourier analysis but the signal is not conspicuous.) We here emphasize orthonormality since only with orthogonal basis can multiscale energy be faithfully defined; the "energy" with a nonorthogonal basis is not physically consistent in that it does not sum over scale levels to the energy in physical space. This is because the required Parseval relation holds only for orthogonal bases.

The resulting spectra are plotted in Fig. 12. For easy reference, the scale level $j = 8$ (32 days) is marked in white in the subplots. From the figure the 154°E series is by far the most energetic. It has a broad spectrum: Energy peaks exist from $j = 1$ (~11 years) to $j = 8.5$ (~22 days) (recall the mean has been removed). The $j = 1$ or decadal oscillation is a well studied feature; it has attracted much interest ever since a long time ago (e.g., Latif and Barnett, 1994; Schneider et al., 2002; Qiu et al., 2013; Taguchi et al., 2010; Pierini, 2014). Remarkably, a substantial portion of variabilities on intraseasonal scales have an energy density comparable to that of the decadal oscillation. The highest scale levels (up to $j = 8.5$ or 22 days) are consistent with results with the absolute instability model (23–27 days; see Table 1).

The other two series have much narrower spectra. In the 164°E spectrum, the highest scale levels for the most energetic variabilities are below 8, and on average they are at about 7.5 (about 45 days). In the 174°E one, they are located even lower, approximately at 6.8 (about 74 days). This is in contrast to that in the 154°E spectrum, where most of the highest levels are above 8. That is to say, in the power spectrum the smallest scale of the energetic intraseasonal variabilities increases eastward with longitude. This is consistent with the results in Table 1. Besides, the corresponding scales agree well with periods of the corresponding local absolute instability waves, except for the 164°E section, where some discrepancy exists.

A conspicuous feature in all the three spectra is the significant part of energy at the highest scale levels or smallest scales, i.e., one day or two; more conspicuously is the big gap between it and that for the intraseasonal processes. Considering that KEx is just below the Pacific storm track, this could be due to the synoptic storms. However, storms have a life cycle of a week or so, while these variabilities have a scale much shorter. Other possibilities include tides, inertial gravity waves, or submesoscale processes (McWilliams, 2016), etc. Whether this is true and how this may function deserve a careful study in the future.

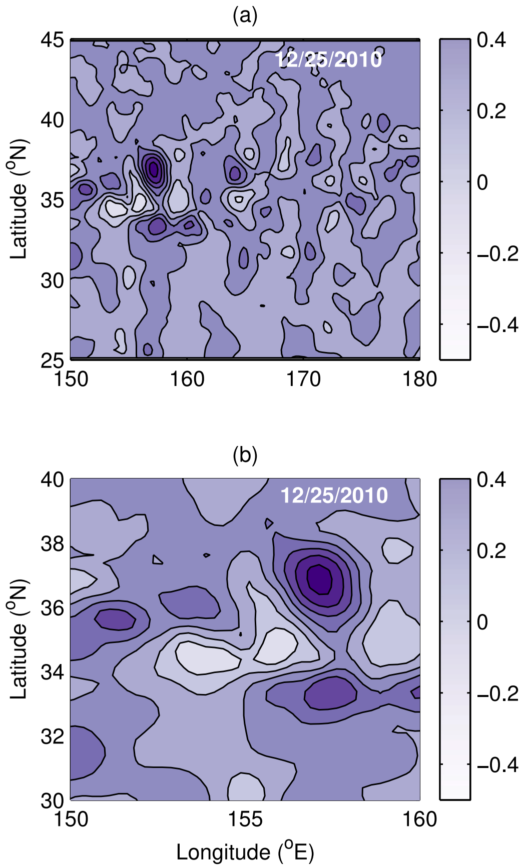

Fig. 11. Reconstructed SSH on the absolute instability window (j = 7–8). (b) is a zoom of (a) on the enhanced eddy region. The units are in meters.

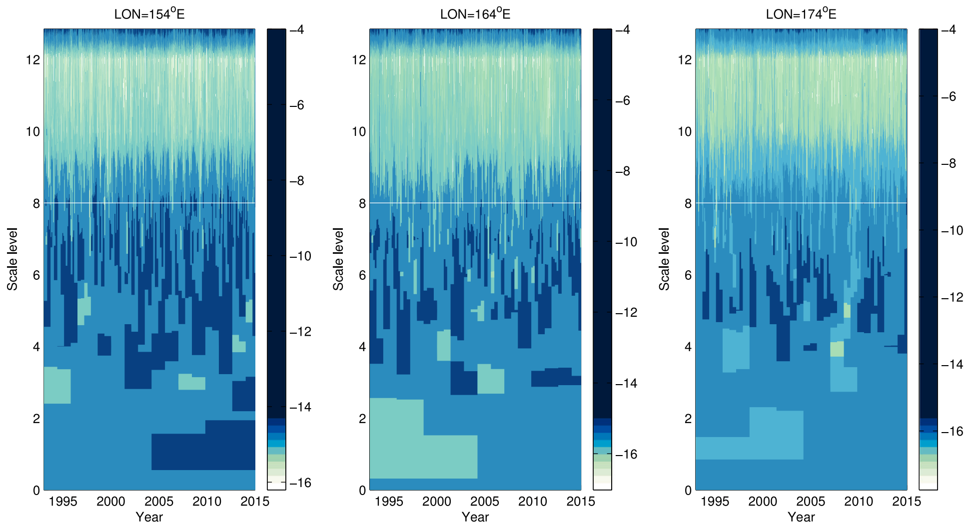

Fig. 12. Wavelet power spectra of the AVISO SSH series at (154°E, 33.125°N), (164°E, 33.125°N), and (174°E, 33.125°N). Shown is the logarithm of the energy in the time-scale domain. The analysis is with an orthonormal wavelet basis generated in Liang and Anderson (2007). The white line marks the scale level 8 (32 days). The mean and annual cycle have been removed from the series prior to the analysis.

5. Discussion and conclusions

Satellite observations have long revealed to us a spatially developing Kuroshio Extension (KEx). However, the underlying convective and absolute instabilities and their associated properties have been mostly overlooked. In this study, we constructed a normal mode instability model to address this issue. We chose a domain east of 150°E, particularly a domain between 154–164°E, to avoid the meandering mean axis in the upstream. Sections at three longitudes are particularly paid attention to: 154°E, 164°E, and 174°E. We used the ECCO data to form the corresponding basic flow profiles. It is found that the basic flow is unstable at these sections, and is all absolutely unstable. In each of the resulting complex dispersion relation diagrams there lies a single saddle point associated with a positive temporal growth rate, which implies self-sustained oscillations. By calculation the absolute instability wave has a frequency decreasing eastward with longitude (corresponding to an increasing period from about 27 days to 72 days), and a slightly increasing wavenumber (corresponding to an slightly decreasing wavelength from 360 km to 250 km). As KEx travels downstream, the associated eigen-structure of the perturbation velocity changes from a surface trapped mode to a mode with components trapped in the vertical interior.

The above absolute instability modes have been evidenced in the wavelet power spectra and multiscale window reconstructions of the AVISO daily SSH data along the KEx axis. In the spectra, it is found that there is substantial energy on the intraseasonal scales and the energy density is comparable to that on larger scales (up to the decadal scale). At least a portion of these variabilities, particularly those on the highest frequencies on this scale window, reveal distinctly different propagation properties from those on larger scales. On the Hovmöller diagram, the fluctuations may appear in the form of stationary waves, or even propagate eastward (rather than westward like Rossby waves). This is the very indication of the absolute instability waves. Besides, the highest frequencies on the window agree with the scales as predicted with the instability model (resp. ~27, 57, 72 days). The observed typical wavelength (~364 km) in some pronounced disturbance region is also comparable to the computed 360 km for that region. We may therefore safely say that this portion of intraseasonal variabilities are generated through absolute instabilities.

Several issues remain. First the meandering axis of the upstream KEx must have large impact on the instability properties. This, however, may preclude a simple basic geostrophic flow and hence introduce, in addition to the complexity of the equations themselves, much difficulty to the instability analysis. As a first step, the present model chooses to avoid this effect, but a sophisticated KEx instability model should eventually take this into account.

An observation is that the frequency of the absolute instability mode increases eastward, while from the Hovmöller diagram the perturbation amplitude decreases with longitude. Does amplitude vary with frequency here? A linear theory cannot tell how amplitude varies—amplitude is determined by initial conditions. But, in this case, is it possible that it be the zonal structure of a global mode? If so, then how frequency is selected with the global mode? Does the selection rely on the local absolute instability structures? These questions, among others, are essentially about how locally unstable flows may give rise to globally instabilities, and for sure deserve a careful investigation. Indeed, the stream here looks like globally unstable. This means it has a finite region of absolute instability (cf. Table 1). In this scenario, by Huerre and Monkewitz (1990), the globally unstable frequency (and complex wave number) is the one measured at the streamwise location, say x_0, where the temporal growth attains its maximum, i.e., where $\left.\frac{d(-\sigma_i)}{dx}\right|_{x=x_0} = 0$. By Table 1, this is likely to occur west of the domain under consideration, i.e., in a region where the Kuroshio Extension meanders. So, again, the investigation cannot proceed without taking in account the meandering axis in the upstream. We look forward to a detailed study in the near future.

CRediT authorship contribution statement

X. San Liang: Conceptualization, Methodology, Theory, Investigation, Writing. **Jianyu Hu:** Investigation, Writing.

Declaration of competing interest

The authors declare that they have no known competing financial interests or personal relationships that could have appeared to influence the work reported in this paper.

Acknowledgments

The comment from an anonymous reviewer on global instability is appreciated. Thanks are due to the ECCO and AVISO groups for making the data available, and to LINPACK for providing the eigenvalue Fortran solver. XSL was originally motivated by a figure kindly supplied by Bo Qiu showing the drifter trajectories in the Kuroshio Extension region. At the early stage of this study, Yang Yang helped download the data and prepared some of the basic flow profiles. This research was jointly supported by the National Natural Science Foundation of China (41276032, 91958203, 41776027) and the 2015 Jiangsu Program for Innovation Research and Entrepreneurship Groups. XSL's visit to Xiamen University was supported by the MEL Visiting Fellowship (MELRS1720).

References

Barnett, T., Pierce, D., Saravanan, R., Schneider, N., Domenget, D., Latif, M., 1999. Origins of the midlatitude Pacific decadal variability. Geophys. Res. Lett. 26, 1453–1456.

Bers, A., 1975. Linear waves and instabilities. In: DeWitt, C., Peyraud, J. (Eds.), Physique Des Plasmas. Gordon & Breach, New York, NY, pp. 117–215.

Briggs, R.J., 1964. Electron-Stream Interaction with Plasmas. MIT Press, Cambridge, MA.

Ceballos, L., Lorenzo, E.D., Hoyos, C., Schneider, N., Taguchi, B., 2009. North Pacific gyre oscillation synchronizes climate fluctuations in the eastern and western boundary systems. J. Clim. 22, 5163–5174.

Chelton, D.B., Schlax, M.G., 1996. Global observations of oceanic Rossby waves. Science 272, 234–238.

Chomaz, J., Huerre, P., Redekopp, L., 1988. Bifurcation to local and global modes in spatially developing flows. Phys. Rev. Lett. 60, 25–28.

DelSole, T., 1997. Absolute instability induced by dissipation. J. Atmos. Sci. 54 (21), 2586–2595.

Deser, C., Alexander, M., Timlin, M., 1999. Evidence for a wind-driven intensification of the kuroshio current extension from 1970s to the 1980s. J. Clim. 12, 1697–1706.

Held, I.M., Pierrehumbert, R.T., Panetta, R.L., 1986. Dissipative destabilization of external rossy waves. J. Atmos. Sci. 43, 388–396.

Hogg, N., 1976. On spatially growing baroclinic waves in the ocean. J. Fluid Mech. 78, 217–235.

Hogg, A., Killworth, P., Blundell, J., Dewar, W., 2005. Mechanisms of decadal variability of the wind-driven ocean circulation. J. Phys. Oceanogr. 35, 512–531.

Huerre, P., Monkewitz, P.A., 1990. Local and global instabilities in spatially developing flows. Annu. Rev. Fluid Mech. 22, 473–537.

Ikeda, M., Apel, J., 1981. Mesoscale eddies detached from spatially growing meanders in an eastward oceanic jet using a two-layer quasi-geostrophic model. J. Phys. Oceanogr. 11, 1638–1661.

Kida, S., coauthors, 2015. Oceanic fronts and jets around Japan: a review. J. Oceanogr. 71 (5), 469–497. http://dx.doi.org/10.1007/s10872-015-0283-7.

Kwon, Y.-O., Deser, C., 2007. North Pacific decadal variability in the community climate system model version 2. J. Clim. 20, 2416–2433.

Latif, M., Barnett, T.P., 1994. Causes of decadal climate variability over the North Pacific and North America. Science 266 (5185), 634–637. http://dx.doi.org/10.1126/science.266.5185.634.

Liang, X.S., Anderson, D.G.M., 2007. Multiscale window transform. SIAM J. Multiscale Model. Simul. 6, 437–467.

Liang, X.S., Robinson, A.R., 2013. Absolute and convective instabilities and their roles in the forecasting of large frontal meanderings. J. Geophys. Res. 118, 1–17.

Lifshitz, E., Pitaevskii, L., 1981. Physical Kinetics. Pergamon, London.

Lindzen, R.S., Farrell, B., 1983. Absolute barotropic instability and monsoon depression. J. Atmos. Soc. 40, 1178–1184.

McCalpin, J., Haidvogel, D., 1996. Phenomenology of the low-frequency variability in a reduced gravity quasigeostrophic double-gyre model. J. Phys. Oceanogr. 26, 739–752.

McWilliams, J.C., 2016. Submesoscale currents inthe ocean. Proc. R. Soc. Lond. Ser. A Math. Phys. Eng. Sci. 472, 20160117.

Merkine, L.O., 1977. Convective and absolute instability of baroclinic eddies. Geophys. Astrophys. Fluid Dyn. 9, 129–157.

Miller, A.J., Chai, F., Chiba, S., Moisan, J.R., Neilson, D.J., 2004. Decadal-scale climate and ecosystem interactions in the North Pacific Ocean. J. Oceanogr. 60 (1), 163C188. http://dx.doi.org/10.1023/B:JOCE.0000038325.36306.95.

Mizuno, K., White, W.B., 1983. Annual and interannual variability in the kuroshio current system. J. Phys. Oceanogr. 13 (10), 1847C1867. http://dx.doi.org/10.1175/1520-0485(1983)013<1847:AAIVIT>2.0.CO;2.

Nakamura, H., Shimpo, A., 2004. Seasonal variations in the southern hemisphere storm tracks and jet streams as revealed in a reanalysis dataset. J. Clim. 17 (9), 1828C1844. http://dx.doi.org/10.1175/1520-0442(2004)017<1828:SVITSH>2.0.CO;2.

Nishikawa, H., Yasuda, I., 2008. Japanese sardine (Sardinops melanostictus) mortality in relation to the winter mixed layer depth in the Kuroshio Extension region. Fish. Oceanogr. 17 (5), 411C420. http://dx.doi.org/10.1111/j.1365-2419.2008.00487.x.

Nishikawa, H., Yasuda, I., 2011. Long-term variability of winter mixed layer depth and temperature along the Kuroshio jet in a high-resolution ocean general circulation model. J. Oceanogr. 67 (4), 503C518. http://dx.doi.org/10.1007/s10872-011-0053-0.

Nonaka, M., Nakamura, H., Tanimoto, Y., Kagimoto, T., Sasaki, H., 2006. Decadal variability in the kuroshio-oyashio extension simulated in an eddy-resolving OGCM. J. Clim. 19.

Pedlosky, J., 1979. Geophysical Fluid Dynamics. Springer, New York.

Penduff, T., Barnier, B., Zika, J., Dewar, W., Treguier, A., Molines, J., Audiffren, N., 2011. Sea level expression of intrinsic and forced ocean variabilities at interannual time scales. J. Clim. 24, 5652–5670.

Pier, B., 2008. Local and global instabilities in the wake of a sphere. J. Fluid Mech. 603, 39–61.

Pierini, S., 2006. A kuroshio extension system model study: decadal chaotic self-sustained oscillations. J. Phys. Oceanogr. 36 (8), 1605–1625.

Pierini, S., 2014. Kuroshio extension bimodality and the north Pacific oscillation: A case of intrinsic variability paced by external forcing. J. Clim. 27 (1), 448–454.

Pierini, S., Dijkstra, H.A., Riccio, A., 2009. A nonlinear theory of the kuroshio extension bimodality. J. Phys. Oceanogr. 39 (9), 2212–2229.

Pierrehumbert, R.T., 1984. Local and global baroclinic instability of zonally varying flow. J. Atmos. Sci. 41, 2141–2162.

Polvani, L., Pedlosky, J., 1988. The effect of dissipation on spatially growing nonlinear baroclinic waves. J. Atmos. Sci. 45, 1977–1989.

Primeau, F., Newman, D., 2008. Elongation and contraction of the western boundary current extension in a shallow-water model: A bifurcation analysis. J. Phys. Oceanogr. 38 (7), 1469–1485.

Qiu, B., 2003. Kuroshio extension variability and forcing of the Pacific decadal oscillations: Responses and potential feedback. J. Phys. Oceanogr. 33, 2465–2482.

Qiu, B., Chen, S., 2010. Eddy-mean flow interaction in the decadally modulating Kuroshio extension system. Deep-Sea Res. II 57 (13–14), 1098–1110.

Qiu, B., Chen, S., Schneider, N., Taguchi, B., 2013. A coupled decadal prediction of the dynamic state of the Kuroshio extension system. J. Clim. 27 (4), 1751C1764. http://dx.doi.org/10.1175/JCLI-D-13-00318.1.

Robinson, A.R., 1999. Forecasting and simulating coastal ocean processes and variabilities with the Harvard Ocean Prediction System. In: Mooers, C.N.K. (Ed.), *Coastal Ocean Prediction*. In: AGU Coastal and Estuarine Studies Series, American Geophysical Union, 1999, pp. 77–100.

Sasai, Y., Richards, K.J., Ishida, A., Sasaki, H., 2010. Effects of cyclonic mesoscale eddies on the marine ecosystem in the Kuroshio extension region using an eddy-resolving coupled physical-biological model. Ocean Dyn. 60 (3), 693C704. http://dx.doi.org/10.1007/s10236-010-0264-8.

Sasaki, Y.N., Minobe, S., Schneider, N., 2012. Decadal response of the kuroshio extension jet to Rossby waves: Observation and thin-jet theory. J. Phys. Oceanogr. 43, 442–456.

Sasaki, Y.N., Schneider, N., 2011. Decadal shifts of the kuroshio extension jet: Application of thin-jet theory. J. Phys. Oceanogr. http://dx.doi.org/10.1175/2011JPO4550.1.

Schneider, N., Miller, A.J., Pierce, D.W., 2002. Anatomy of North Pacific decadal variability. J. Clim. 15 (6), 586C605.

Seager, R., Kushnir, Y., Naik, N., Cane, M., Miller, J., 2001. Wind-driven shifts in the latitude of the Kuroshio-Oyashio Extension and generation of SST anomalies on decadeal timescales. J. Clim. 14, 4249–4265.

Simonnet, E., Dijkstra, H., 2002. Spontaneous generation of low-frequency modes of variability in the wind-driven ocean circulation. J. Phys. Oceanogr. 32, 1747–1762.

Taguchi, B., Qiu, B., Nonaka, M., Sasaki, H., Xie, S.-P., Schneider, N., 2010. Decadal variability of the Kuroshio-Extension: Meso-scale eddies and recirculations. Ocean Dyn. 60, 673–682.

Thacker, W.C., 1976. Spatial growth of Gulf Stream meanders. Geophys. Fluid Dyn 7, 271–295.

Thual, S., Thual, O., Dewitte, B., 2013. Absolute or convective instability in the equatorial Pacific and implications for ENSO. Quart. J. R. Meteorol. Soc. 139, 600–606.

Wang, Y.-H., Liu, W.T., 2015. Observational evidence of frontal-scale atmospheric responses to kuroshio extension variability. J. Clim. 28 (23), 9459–9472. http://dx.doi.org/10.1175/JCLI-D-14-00829.1.

Wijffels, S., Hall, M., Joyce, T., Torres, D.J., Hacker, P., Firing, E., 1998. Multiple gyres of the western North Pacific: a WOCE section along 1491E. J. Geophys. Res. 103, 12985–13009.

Wong, R., 2001. Asymptotic approximations of integrals. In: Classics in Applied Mathematics, Vol. 34. SIAM, Philadelphia, PA, p. xviii+543.